



Optical properties of high temperature molten salt mixtures for volumetrically absorbing solar thermal receiver applications



Melanie Tetreault-Friend^{a,*}, Luke A. Gray^b, Shapagat Berdibek^a, Thomas McKrell^a, Alexander H. Slocum^b

^a Department of Nuclear Science and Engineering, Massachusetts Institute of Technology, 77 Massachusetts Avenue, Cambridge, MA, 02139, USA

^b Department of Mechanical Engineering, Massachusetts Institute of Technology, 77 Massachusetts Avenue, Cambridge, MA, 02139 USA

ARTICLE INFO

Article history:

Received 20 December 2016

Received in revised form 12 May 2017

Accepted 15 May 2017

Keywords:

Optical properties

Molten salts

Fluids

Radiative heat transfer

Solar thermal energy

ABSTRACT

Molten salts are promising candidates for liquid volumetric absorbers in concentrated solar power systems. To characterize absorption and heat transfer performance in high temperature applications, their optical properties are required. Thus a method for experimentally determining the absorption coefficient of non-scattering high temperature semi-transparent liquids for large (~1 m-deep) direct absorption solar receiver applications was developed. It was used to measure the absorption coefficient in liquids over a broad spectral range and temperatures up to 800 °C in a 40 wt.% KNO₃:60 wt.% NaNO₃ binary nitrate molten salt mixture (solar salt) and a 50 wt.% KCl:50 wt.% NaCl binary chloride molten salt mixture. The binary nitrate and binary chloride both demonstrated well distributed solar absorption (>95% absorption through 1 m and 2 m, respectively). At 400 °C, the binary nitrate is optically thick in its re-emission spectrum and behaves as a blackbody radiator. The effects of thermal decomposition were also shown to have significant consequences on the overall performance of the binary nitrate mixture, transforming it into an opaque surface absorber following thermal degradation (>95% in <0.25 m). The implications of these results for solar receiver design are discussed in terms of volumetric absorption, total effective emissivity, and capture efficiency. The measurement technique developed and results are relevant in a variety of high temperature applications including heat transfer systems, materials processing, pharmaceuticals, and food processing facilities.

© 2017 Elsevier Ltd. All rights reserved.

1. Introduction

Typical solar collectors absorb incident solar radiation through surface absorbers before transferring this radiation as thermal energy to a working fluid or storage material. Volumetric receivers using direct volumetrically absorbing fluids promise significant performance enhancement over current surface absorber designs and lead to increased efficiency (Khullar et al., 2014; Lenert and Wang, 2012; Ni et al., 2016). In particular, the Concentrated Solar Power on Demand (CSPonD) concept (Slocum et al., 2011) is a system which consists of a collocated volumetrically absorbing molten salt solar receiver with inherent thermal energy storage. The simultaneous use of a volumetrically absorbing high temperature fluid as storage medium and working fluid is an alternative solar absorption approach which allows incident solar radiation to be directly absorbed and stored by the working fluid and eliminates the need for intermediate surface absorbers. The candidate molten salts generally behave as semi-transparent, radiatively participating liquids which do not necessarily require nanoengineered parti-

cle suspensions to tailor their optical properties (Lenert and Wang, 2012). Radiative heat transfer is therefore expected to be a dominating mechanism for heat absorption and transport within the salts and their optical properties are required to characterize their thermal behavior.

The CSPonD Demo prototype (Gil et al., 2016) uses a 40 wt.% KNO₃:60 wt.% NaNO₃ binary nitrate molten salt mixture (solar salt) for which measured absorption properties are only available for wavelengths from 400 nm to 800 nm (Passerini, 2010) in high purity salts that do not accurately capture the behavior of commercial salts used under real operating conditions. In contrast with the typically smaller volumetrically absorbing solar receiver designs and the associated optical property data available (Drotning, 1978; Viskanta and Anderson, 1975; Webb and Viskanta, 1985), Slocum et al. have proposed a large scale commercial CSPonD design 5 m deep × 25 m diameter and consider the use of chloride salts which commonly operate at 900 °C. Ideal solar penetration depths for such volumetrically absorbing systems should closely match the depth of the absorber liquid, requiring the ability to measure nearly-transparent high-temperature materials. However, typical methods for measuring the optical properties of liquids use reflectance techniques (Makino et al., 1991; Myers et al., 2015)

* Corresponding author.

E-mail address: mtfriend@mit.edu (M. Tetreault-Friend).

Nomenclature

List of symbols

A_m	solar-weighted absorption factor	q_s	surface radiative heat flux
C	solar concentration	R	surface reflectance
$C_1 = 3.7418 \times 10^{20} \text{ W} - \text{nm}^4/\text{m}^2$	first radiation constant	T	temperature
$C_2 = 14388.69 \times 10^3 \text{ nm} - \text{K}$	second radiation constant	\bar{T}_{op}	mean fluid operating temperature
E_{λ_o}	spectral solar irradiance	Δx_i	fluid path length
$\bar{E}_{solar} = E_{\lambda_o}/E_{\lambda_o,max}$	normalized solar spectral irradiance	$\beta(T, \lambda_o)$	attenuation coefficient
$I_i(T, \lambda_o)$	spectral intensity	$\epsilon(L_{e,E}, \bar{T}_{op})$	total emissivity of isothermal fluid layer
$I_o(\lambda_o)$	incoming light source intensity	$\eta_{capture}$	capture efficiency
$I_{b_i}(\bar{T}_{op})$	spectral emissive blackbody intensity inside the fluid	κ	absorption coefficient
$\hat{I}_{b_i, \bar{T}_{op}} = I_{b_i}(\bar{T}_{op})/I_{b,max}(\bar{T}_{op})$	normalized blackbody intensity spectra	κ_{MS}	solar-weighted absorption coefficient
L	actual thickness of fluid layer	κ_{ME}	re-emission-weighted absorption coefficient
L_m	average mean beam length	λ_o	vacuum wavelength
$L_{e,S}$	mean beam length through fluid thickness in solar spectrum	$\lambda = \frac{\lambda_o}{n}$	wavelength inside medium
$L_{e,E}$	mean beam length through fluid thickness in re-emission spectrum	σ	boltzmann constant
n	index of refraction	$\sigma_s(T, \lambda_o)$	scattering coefficient
		τ	optical thickness
		τ_{MS}	solar-weighted optical thickness
		τ_{ME}	re-emission-weighted optical thickness

with small sample thicknesses (≤ 10 mm). The measurement resolution for these techniques is typically $>100 \text{ m}^{-1}$ which does not accurately capture the properties of nearly transparent liquids. In addition, these techniques are often used in conjunction with spectrometers (Otanicar et al., 2009; Passerini, 2010; Passerini and McKrell, 2012) which do not provide accurate measurements for high temperature materials at infrared wavelengths. The high operating temperatures also suggest participating media effects within the salts are non-negligible, further emphasizing the necessity of measuring optical properties over a wide spectral range extending into the mid-infrared spectrum. It is therefore of great value to characterize the solar absorption, the internal re-emission, and the radiative losses for these systems at elevated temperatures.

In this work, we present a simple and accurate apparatus that allows for the precise measurement of light attenuation in high temperature, nearly transparent liquids, over a broad spectrum extending from the visible region (400 nm) into mid-infrared (8 μm). The apparatus is used to measure the attenuation of light in the 40 wt.% KNO_3 :60 wt.% NaNO_3 binary nitrate and the 50 wt.% KCl :50 wt.% NaCl binary chloride molten salt mixtures. The attenuation measurements provide direct insight into the absorption properties of non-scattering liquids. The effects of salt contamination due to thermal decomposition are also evaluated. Sources of contamination in the CSPonD include thermal decomposition due to unexpected heating conditions and local hot spots, and sand/dust contamination due to the open receiver design. The implications of the results are discussed in the context of the CSPonD Demo and for general volumetrically absorbing solar receiver applications.

2. Experimental procedure

2.1. Apparatus description

The attenuation coefficient is a function of temperature and wavelength and is expressed in terms of absorption and scattering as:

$$\beta(T, \lambda_o) = \kappa(T, \lambda_o) + \sigma_s(T, \lambda_o) \quad (1)$$

where $\beta(T, \lambda_o)$ is the attenuation coefficient, $\kappa(T, \lambda_o)$ is the absorption coefficient, and $\sigma_s(T, \lambda_o)$ is the scattering coefficient, each eval-

uated at temperature T and (vacuum) wavelength λ_o . There are several ways of measuring the attenuation coefficient (Modest, 2013; Myers et al., 2015; Otanicar et al., 2009; Passerini and McKrell, 2012). The method selected in this work evaluates the attenuation coefficient by measuring and comparing the transmission of light through different material thicknesses and relating them via the Beer-Lambert's Law:

$$\beta(T, \lambda_o) = \frac{-1}{\Delta x_j - \Delta x_i} \ln \left(\frac{I_j(T, \lambda_o)}{I_i(T, \lambda_o)} \right) \quad (2)$$

where $I_i(T, \lambda_o)$ and $I_j(T, \lambda_o)$ are the transmitted outgoing intensities measured by the FTIR detector for corresponding path lengths Δx_i and Δx_j through the fluid at temperature T , for a constant collimated incoming light source $I_o(T, \lambda_o)$ perpendicularly incident to the cuvette windows. The attenuation can therefore be calculated from any combination of measured outgoing intensities.

To carry out the optical measurements, the furnace based apparatus developed by Passerini (Passerini, 2010; Passerini and McKrell, 2012) was modified and adapted to be used in conjunction with a Bruker VERTEX 70 Fourier Transform Infrared (FTIR) spectrometer with a 150 W tungsten lamp externally adapted light source, which replaces the integrating sphere and spectrometer in the original experimental setup. FTIRs operate over a much wider spectral range than dispersive infrared spectrometers used in previous studies. One of the main disadvantages of dispersive methods is that the radiation emitted by the apparatus at high temperatures inevitably contributes to the overall IR radiation signal for temperatures above 700 °C. To circumvent this challenge, the FTIR uses a Michelson Interferometer to modulate the source and differentiate it from the unmodulated high temperature emissions.

The apparatus consists of a vertically oriented and electrically heated split tube furnace, as shown in Fig. 1a. Two coaxial quartz cuvettes are positioned inside the furnace. Both cuvettes are closed at the bottom with fire polished quartz windows. The sample fluid is added to the outer cuvette only and the inner cuvette is partially immersed in the fluid and has an adjustable vertical position. Attenuation measurements can therefore easily be made for different fluid thicknesses by adjusting the inner cuvette's height. Relevant applications call for semi-transparent fluids 1 m in depth and optical thickness $\tau \approx 1$. The FTIR can readily resolve attenuations

on the order of 5%. Heights of up to 10 cm therefore provide sufficient attenuation to measure the nearly transparent salt's attenuation coefficient for pertinent applications. The double cuvette design is also advantageous because it minimizes vibrational issues by eliminating the free surface of the fluid from the beam path. A schematic of the apparatus is shown in Fig. 1.

As illustrated in Fig. 1b, the outgoing intensities are measured by the FTIR detector for different path lengths through the liquid. The selected double cuvette design and method for calculating attenuation coefficient eliminate the effects of surface reflections at the cuvette interfaces and any effects from precipitates at the bottom of the cuvette. Reflections and deposits correspond to a constant attenuation in the incoming light source $I_o(T, \lambda_o)$ before being attenuated by the liquid itself for any given path length and do not contribute to volumetric attenuation. Because only transmitted intensities are required in Eq. (2), these effects therefore need not be quantified to evaluate the attenuation coefficient. At 800 °C, the intensity of the thermal radiation emitted by the surface of the hot salts in the near-infrared spectrum exceeded the operating range and saturated the FTIR detector. A radiation shield was therefore required to carry out the measurements. The radiation shield is made of extra high temperature silica ceramic insulation material wrapped in aluminum foil with a small aperture in the center allowing the transmitted to pass through, as shown in Fig. 1a. The design can also be used in wavelengths between 2.5 μm and 5.0 μm where quartz is only partially transmissive since its attenuation is constant at all path lengths. For measurements at wavelengths greater than 5.0 μm , the quartz windows would be replaced with a more optically transmissive window material such as diamond, zinc selenide, or calcium fluoride. Window material selection will also depend on its compatibility with the measured fluid.

2.2. Mixture preparation

Refined grade sodium and potassium nitrate salts (>99.5% purity) were provided by SQM Corp. and pre-mixed to obtain a 40 wt.% KNO_3 :60 wt.% NaNO_3 binary nitrate molten salt mixture. Sodium and potassium chloride salts (>99.0% purity) were purchased separately from Alfa Aesar (product numbers #12314 and #11595) and pre-mixed to obtain a 50 wt.% KCl :50 wt.% NaCl binary chloride molten salt mixture. None of the salts contained anti-caking agents. A new batch of salt was prepared for each set of measurements and any variations in the salt preparation are reflected in the reported repeatability uncertainty.

The salts are then dried in an oven at 50 °C for at least 1 h to remove excess moisture before being loaded in the outer cuvette.

A K-type thermocouple positioned at the mid-height of the furnace on the outer wall of the outer cuvette is connected to a temperature controller which controls the furnace output and allows the salts to be heated at a slow and steady rate to a set temperature. Passerini and McKrell (2012) characterized the axial variation in temperature along the outer cuvette and reported a maximum deviation of 10%. Nevertheless, the measured properties had only a very weak dependence on temperature as is discussed in Section 4 and a 10% deviation is expected to have a negligible effect, even at higher temperatures.

Irregular operating conditions may be expected to introduce thermal decomposition from unexpected heating conditions and local hot spots in the salts, and preliminary characterization of its effects was carried-out. For example, decomposition of the binary nitrate molten salt mixture was achieved by raising the temperature of the molten salt to 550 °C (open system decomposition temperature (Alqaydi et al., 2016)) for 45 min. Bubbling was observed during decomposition and the salt developed a green tint.

2.3. Measurement procedure

Once the salt mixture has melted, the inner cuvette is moved to its lowest position corresponding to approximately 1–2 cm of liquid thickness and a transmission spectrum is acquired at each vertical position in 5 mm increments up to 10 cm. The maximum height was selected as a compromise between measurement sensitivity requirements as described in Section 2.1, and experimental apparatus sizing and cost limitations. Once the maximum position is reached, the cuvette is lowered in 5 mm increments and the measurements are repeated to ensure repeatability of the measurement versus depth. In total, measurements were taken twice for 10–20 different path lengths. In addition, the measurements were acquired for three different salt temperatures for the nitrate mixture: 300 °C, 350 °C, and 400 °C, and at 800 °C for the chloride mixture due to its weak temperature dependence as will be discussed. The transmission spectrum scanning resolution is <5 nm. In addition, a moving average filter with a maximum size of 160 cm^{-1} (<20 nm) was used in the visible spectrum to compensate for the noise in the signal.

2.4. Thermal performance evaluation

To understand the thermal behavior of the salt and in particular the radiative heat transfer within the different media, we consider three factors: the general participating media behavior, the volumetric absorption, and the effective emissivity. The latter two

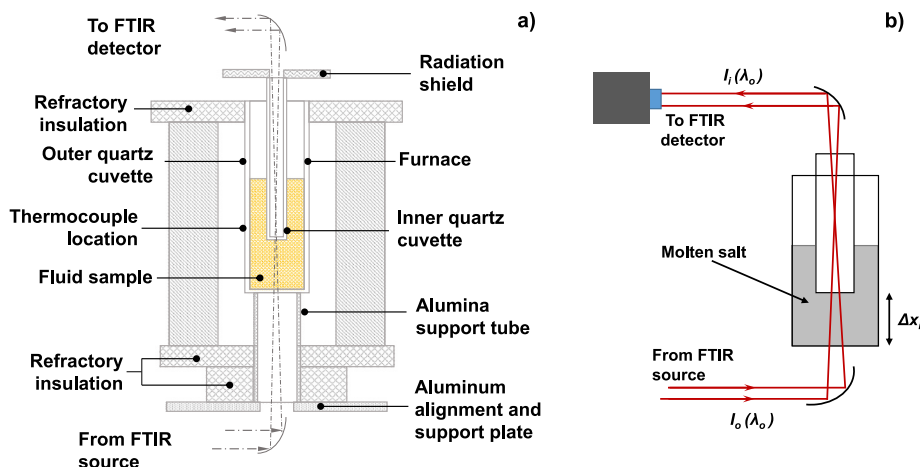


Fig. 1. Simplified diagram of apparatus (a) and variable path length method illustration (b) used to measure the attenuation of light intensity by liquids.

can be considered together in the capture efficiency. We first define solar-weighted and re-emission-weighted absorption coefficients and optical thicknesses for the fluids, given as

$$\kappa_{MS} = \frac{\int_0^\infty E_{\lambda_o} \kappa_{\lambda_o} d\lambda_o}{\int_0^\infty E_{\lambda_o} d\lambda_o}, \quad (3)$$

$$\kappa_{ME} = \frac{\int_0^\infty I_{b\lambda_o}(\bar{T}_{op}) \kappa_{\lambda_o} d\lambda_o}{\int_0^\infty I_{b\lambda_o}(\bar{T}_{op}) d\lambda_o}, \quad (4)$$

$$\tau_{MS} = \kappa_{MS} L_{e,S} \quad \text{and} \quad \tau_{ME} = \kappa_{ME} L_{e,E} \quad (5)$$

where E_{λ_o} is the spectral solar irradiance (ASTM Standard G173–03, 2003), κ_{λ_o} is the measured spectral absorption coefficient of the fluid, $L_{e,S}$ and $L_{e,E}$ are the mean beam lengths through the fluid thickness in the solar and re-emission spectrum, respectively, and $I_{b\lambda_o}(\bar{T}_{op})$ is the spectral emissive blackbody intensity inside the fluid at its average operating temperature \bar{T}_{op} , given by Planck's Law:

$$I_{b\lambda}(\bar{T}_{op}) = \frac{C_1}{\pi n^2 \lambda^5 [e^{C_2/(n\lambda\bar{T}_{op})} - 1]} \quad (6)$$

where C_1 and C_2 are the first and second radiation constants, n is the index of refraction of the fluid, and λ is the wavelength inside the medium, defined as $\lambda = \frac{\lambda_o}{n}$. In the optically thick limit where $\tau \rightarrow \infty$, the medium behaves as an opaque body with negligible participating media effects, and the heat flux at the surface approaches the same value as for a blackbody radiator (Howell et al., 2010; Modest, 2013). In the limit where $\tau \ll 1$, the medium is said to be optically thin and its re-emitted radiation travels long distances without being absorbed. Because the salt mixtures used in this work have high purity levels, we assume scattering to be negligible (Webb and Viskanta, 1985) and take the absorption coefficient to be approximately equal to the measured attenuation coefficient.

The solar absorption can be characterized by evaluating the solar-weighted absorption factor. The value yields the fraction of incoming solar energy absorbed by the medium for a given thickness (Drotning, 1978) and is defined as:

$$A_m = \frac{(1 - R_{norm}) \int_0^\infty E_{\lambda_o} (1 - e^{-\kappa_{\lambda_o} L_{e,S}}) d\lambda_o}{\int_0^\infty E_{\lambda_o} d\lambda_o} \quad (7)$$

where R_{norm} is the normal reflectance at the surface (Appendix C). The radiative losses to the environment are characterized by the total emissivity of an isothermal fluid layer of thickness $L_{e,E}$ given as

$$\epsilon(L_{e,E}, \bar{T}_{op}) = (1 - R_{diff}) \left(\frac{\int_0^\infty I_{b\lambda_o}(\bar{T}_{op}) (1 - e^{-\kappa_{\lambda_o} L_{e,E}}) d\lambda_o}{\int_0^\infty I_{b\lambda_o}(\bar{T}_{op}) d\lambda_o} \right) \quad (8)$$

where R_{diff} is the diffuse reflectance at the surface (Appendix C). The heat flux losses at the surface of the isothermal medium, q_s , can thus be given as

$$q_s = \epsilon(L_{e,E}, \bar{T}_{op}) \sigma \bar{T}_{op}^4 \quad (9)$$

assuming a vacuum boundary condition at the surface, where n is the refractive index of the medium and σ is the Stefan-Boltzmann constant.

Finally, we evaluate the capture efficiency of the medium as

$$\eta_{capture} = \frac{q_{abs} - q_{loss}}{q_{incident}} = A_m - \frac{q_s}{C \int_0^\infty E_{\lambda_o} d\lambda_o} \quad (10)$$

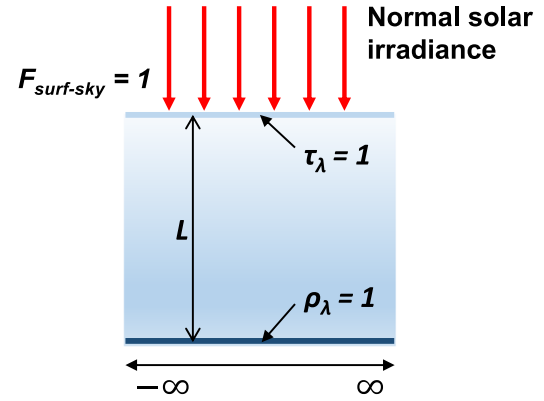


Fig. 2. Diagram illustrating assumptions and boundary conditions for performance evaluation.

where $q_{incident}$ is the incident solar energy, q_{abs} is the absorbed amount of solar energy, q_{loss} are the thermal losses at the surface, and C is the solar concentration factor. In this work, we take the average operating temperature as 400 °C for the binary nitrate and 800 °C for the binary chloride. From the Kramers-Krönig dispersion relations (Hutchings et al., 1992; Kramers, 1927; Kronig, 1926; Modest, 2013), the refractive index has wavelength dependence related to the absorption properties, with only small variations away from the absorption peaks. The chloride based salts are therefore not expected to show large variation in n below 14 μm . Furthermore, experimental evidence from Makino (Makino et al., 1991) confirms negligible n -variation in the nitrate salts for wavelengths below 5 μm . Therefore, the refractive indices are simply taken to be the published values measured at the 589 nm sodium D line, where $n = 1.41$ for eutectic $\text{NaNO}_3\text{-KNO}_3$ (Jindal and Harrington, 1967) and $n = 1.40$ for the mass weighted average properties of the 50 wt.% KCl ($n = 1.417$):50 wt.% NaCl ($n = 1.385$) (Bloom and Rhodes, 1956; Janz, 1967).

In order to characterize the performance of the salt itself, independently of the containment vessel wall's properties, we assume the fluids are contained in infinite slabs with specularly reflective bottom boundary and transmissive top boundary, and solar irradiance normal to the surface of the fluid, as illustrated in Fig. 2. The infinite slab is selected as a generalization which isolates the effects of the salt properties only. Other geometries will introduce boundary effects that are application specific. The mean beam lengths through the fluid are therefore $L_{e,S} = 2L$ for the solar absorption, where L is the actual thickness of the fluid, and $L_{e,E} = 2L_m$ for the re-emission, where L_m is the average mean beam length given by Modest (Modest, 2013) as $L_m = 1.76L$ for an infinite slab.

3. Experimental validation

Using the procedure previously outlined, the spectral absorption coefficient of propylene glycol was measured as a reference for validation and the results are presented in Fig. 3. The experimental results are presented with previously published values (Otanicar et al., 2009). The discontinuity at approximately 833 nm ($12,000 \text{ cm}^{-1}$) corresponds to a switch from a Silicon-Diode detector (visible) to an Indium Gallium Arsenide detector (near infrared). Experimental repeatability and deviations in the measurement resulted in much higher uncertainty than the instrumentation uncertainty (Appendix B). We therefore report the average value of the measurements for each data point with uncertainty expressed as the standard deviation. Experimental repeatability was limited by the salt preparation, optics, and

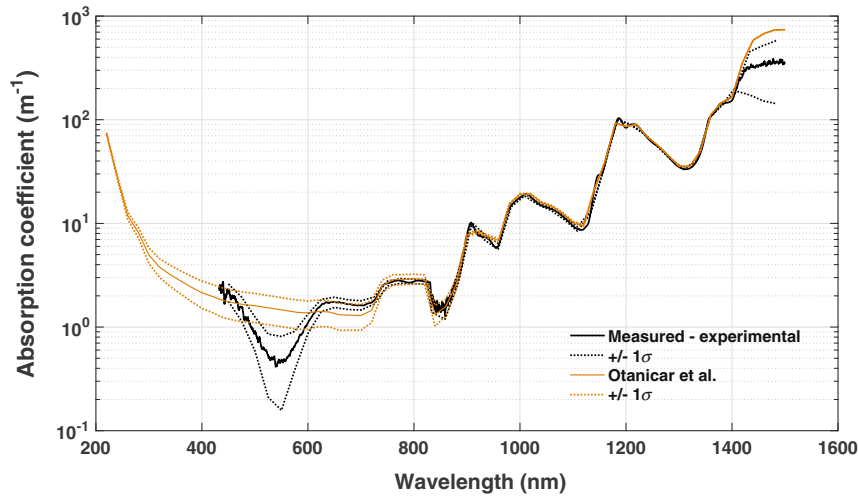


Fig. 3. Experimental results for the absorption coefficient of propylene glycol versus wavelength.

cuvette alignment. The variation in repeatability error over the wavelength range studied depends largely on the sensitivity of the detector, the intensity of the light source, and the transmission through the liquid. The measured results agree well with the published results over the measured spectrum, with some divergence at wavelengths where the transmission reaches extreme values ($\approx 0\%$ or $\approx 100\%$). At these wavelengths, the ratio $\frac{I_j(T, \lambda_o)}{I_i(T, \lambda_o)}$ in Eq. (2) diverges as the measured intensities converge to the same values. The uncertainty is largest and diverges most from the published results between 500 nm and 600 nm where the absorption is on

the order of 1 m^{-1} . Nevertheless, uncertainty due to repeatability in the measurements remains below $\pm 20\%$ at all reported wavelengths. The large error in the nearly transparent region can be reduced by increasing the maximum fluid height measured. The maximum deviation between the measured and published average values is also at this location, where the two deviate 40%. Below 425 nm, the intensity of the light source decays too rapidly to obtain accurate measurements. Above 1400 nm, propylene glycol's absorption approaches large values exceeding 10^3 m^{-1} and becomes too opaque for the sensitivity of the apparatus, but more transparent liquids may still be measured at longer wavelengths.

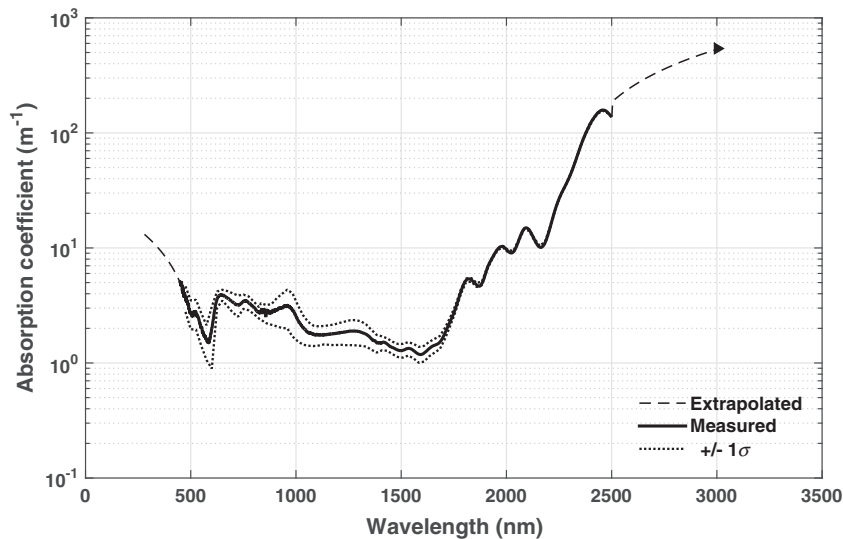


Fig. 4. Absorption coefficient of 40 wt.% KNO_3 :60 wt.% NaNO_3 binary nitrate molten salt (SQM) at 400 °C.

Table 1

Calculated solar- and re-emission-weighted absorption coefficients and optical thicknesses based on measured and extrapolated optical properties with $L = 1 \text{ m}$.

Fluid	κ_{MS} (m^{-1})	κ_{ME} (m^{-1})	τ_{MS} (-)	τ_{ME} (-)
(Na-K) NaNO_3 $\bar{T}_{op} = 400 \text{ }^\circ\text{C}$	12.5	3706.9	24.9	13048.2
Decomposed (Na-K) NaNO_3 $\bar{T}_{op} = 400 \text{ }^\circ\text{C}$	35.1	3792.3	70.2	13348.9
(Na-K)Cl $\bar{T}_{op} = 400 \text{ }^\circ\text{C}$	2.5	0.7	5.0	2.3

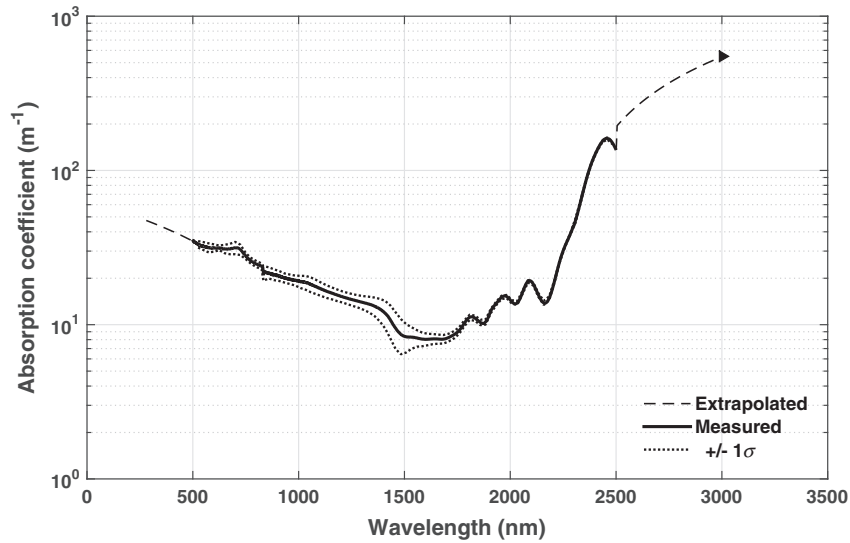


Fig. 5. Absorption coefficient of decomposed 40 wt.% KNO_3 :60 wt.% NaNO_3 binary nitrate molten salt (SQM) at 400 °C.

Previous measurement methods using very thin fluid layers (Drotning, 1978; Makino et al., 1991; Myers et al., 2015) are limited to more opaque fluids, and techniques using spectrophotometers (Otanicar et al., 2009; Passerini and McKrell, 2012) cannot be used at very high temperature. The verified method presented in this study is applicable to a wide range of semi-transparent liquids with no temperature limitations. Given the validation results, the optimal accuracy is achieved for wavelengths above 425 nm and for absorption coefficients between 0.5 m^{-1} and 500 m^{-1} . The method can be used to rapidly measure a series of liquid thicknesses over a much larger range than in previous studies and is particularly relevant for applications involving large depths ($\sim 1 \text{ m}$) of high temperature fluids such as volumetric solar receivers, thermal energy storage systems, glass processing, and salt bath heat treatment facilities.

4. Results

The general behavior of the measured liquids agrees with the Lorentz model for ionic crystals (Lorentz, 1935; Modest, 2013; Smakula, 1962) which is valid for both solids and liquids. The

Lorentz model predicts a long-wavelength absorption edge which is the wavelength at which strong absorption begins due to Reststrahlen bands (photon excitation of lattice vibrations) in the mid-infrared. The model also predicts several absorption bands at short wavelengths (typically in the ultraviolet) which correspond to the excitation of valence band electrons across the band gap into the conduction band.

The measured spectral absorption coefficient at 400 °C for the refined grade 40 wt.% KNO_3 :60 wt.% NaNO_3 binary nitrate molten salt mixture is presented in Fig. 4. In the near-infrared (NIR), the absorption decreases slowly until it reaches a local minimum of 4.5 m^{-1} at approximately 1600 nm. Absorption peaks begin beyond this point and rapidly increase up to 160 m^{-1} at 2500 nm, indicating the onset of Reststrahlen bands. After this point, the absorption band is expected to continue increasing, extending beyond the range of accuracy of measurements. At shorter wavelengths, small peaks appear in the visible spectrum with a sharp increase for wavelengths below 600 nm. This location is expected to indicate the location of a strong short-wavelength absorption band as predicted by the Lorentz model, which is also supported by the measured absorption of other nitrate and nitrite

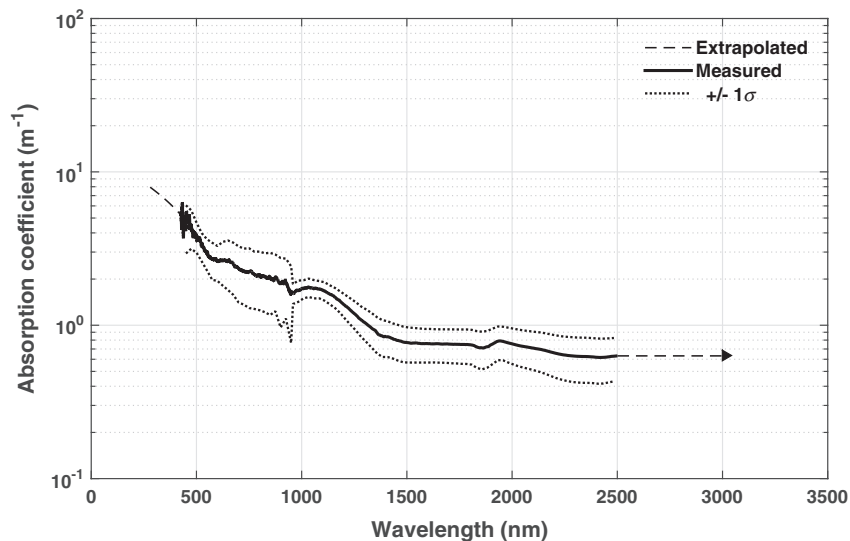


Fig. 6. Absorption coefficient of 50 wt.% KCl :50 wt.% NaCl binary chloride molten salt at 800 °C.

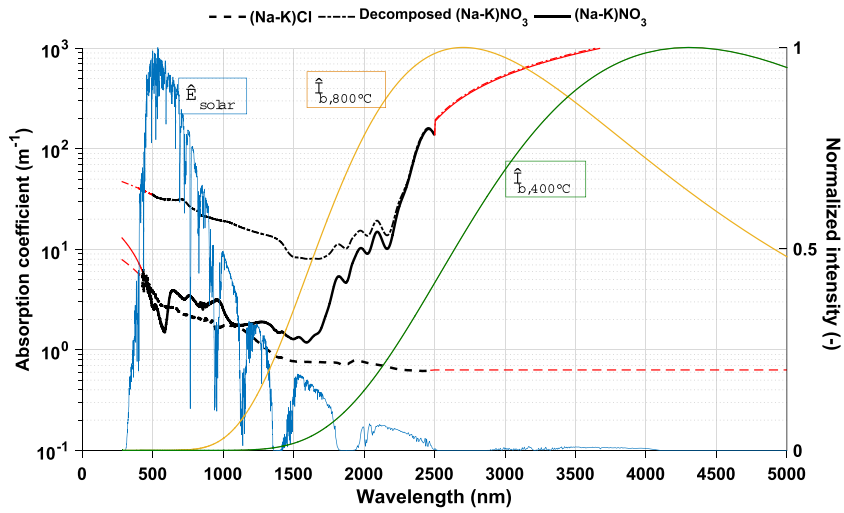


Fig. 7. Absorption coefficient of binary nitrate and decomposed binary nitrate at 400 °C, and binary chloride at 800 °C (log-scale), with corresponding normalized blackbody intensity spectra $I_{b,400^\circ\text{C}}$ and $I_{b,800^\circ\text{C}}$, and normalized solar spectrum E_{solar} (linear-scale).

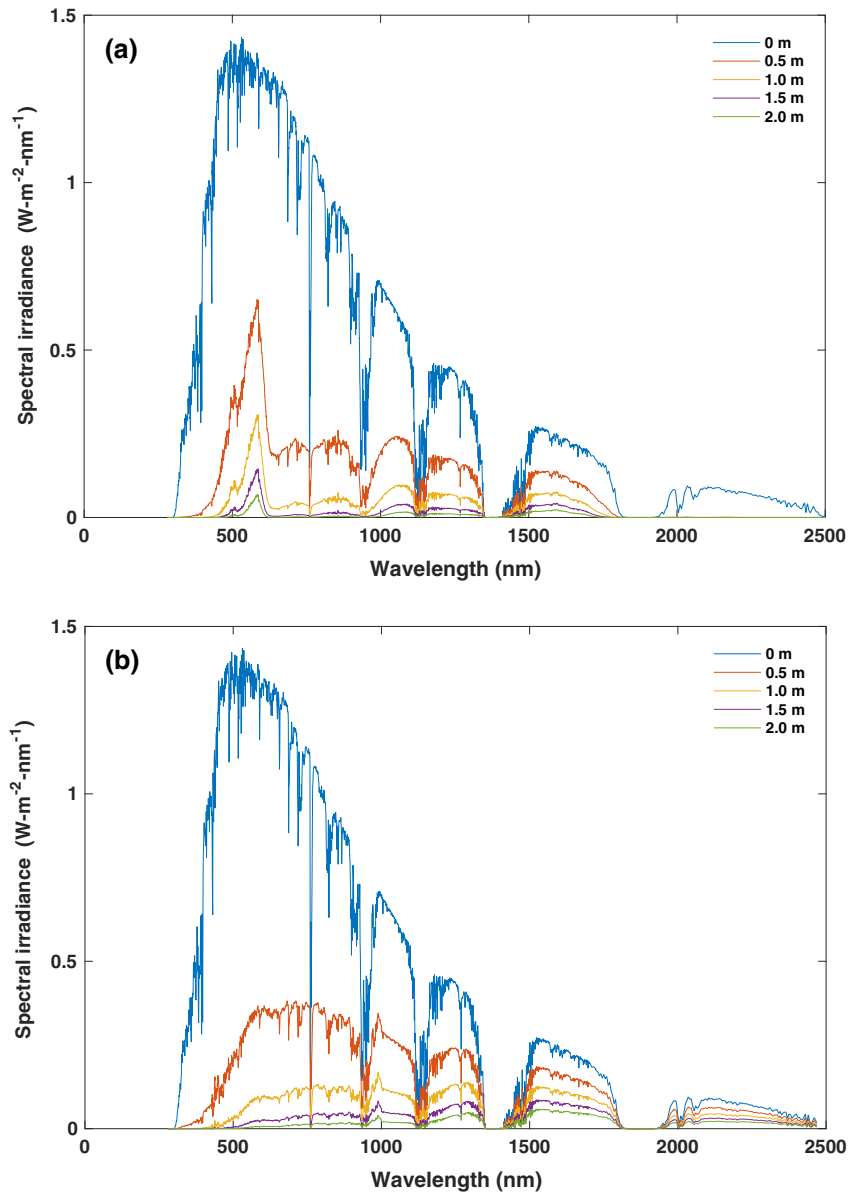


Fig. 8. Solar irradiance distribution at different salt depths for binary nitrate at 400 °C (a), and binary chloride at 800 °C (b).

salts (Drotning, 1978; Makino et al., 1991), and preliminary measurements by Passerini (Passerini, 2010). The measured properties had only a very weak dependence on temperature and are therefore reserved for the appendix (Appendix A). The short-wavelength absorption edge shifts very lightly to longer wavelengths for increasing temperature. A very weak Reststrahlen band (Modest, 2013) shift to shorter wavelengths is also expected but was not observable over the measured temperature range.

Overall, the general behavior can be interpreted from the solar-weighted and the re-emission-weighted absorption coefficients. Using linear extrapolation in the high absorption regions, weighted coefficients were determined to be $\kappa_{MS} = 12.5 \text{ m}^{-1}$ and $\kappa_{ME} = 3706.9 \text{ m}^{-1}$. For a receiver 1 m deep, and corresponding optical thicknesses $\tau_{MS} = 24.9 > 1$ and $\tau_{ME} = 13,048.2 \gg 1$, the fluid behaves as a participating media in the solar spectrum, and is optically thick (blackbody radiator) in the re-emission spectrum at 400 °C (see Table 1).

The measured spectral absorption coefficient at 400 °C for the decomposed 40 wt.% KNO₃:60 wt.% NaNO₃ binary nitrate molten salt mixture is presented in Fig. 5. The location of the long-wavelength absorption edge near 2 μm is unchanged relative to that of the undecomposed nitrate (Fig. 4), but the overall absorption in the NIR and visible spectra increases almost a full order of magnitude. The rapid growth rate with decreasing wavelength in the visible spectrum is lessened relative to the intact mixture and there is no clear absorption edge. Below 500 nm, the absorption became too large for the intensity of the light source to obtain an accurate measurement. Nevertheless, the measured spectrum still captures approximately 84% of the integrated solar energy spectrum. In addition, at this wavelength the absorption approaches large enough values to be approximated as an opaque blackbody radiator for large scale volumetric absorbers such as the CSPOND. The effect of temperature on the measured properties was also negligible in this case (Appendix A). In terms of weighted properties, $\kappa_{MS} = 35.1 \text{ m}^{-1}$ and $\kappa_{ME} = 3792.3 \text{ m}^{-1}$. For a receiver 1 m deep, and corresponding optical thicknesses $\tau_{MS} = 70.2 \gg 1$ and $\tau_{ME} = 13,348.9 \gg 1$, the fluid behaves as a surface absorber in the solar spectrum, and a blackbody radiator in the re-emission spectrum at 400 °C (see Table 1).

The measured properties for the 50 wt.% KCl:50 wt.% NaCl binary chloride molten salt mixture at 800 °C are shown in Fig. 6. We note here that the large uncertainty in the region below 1000 nm is due to the combined effects of the highly transparent nature of the mixture and the reduced measurement sensitivity of the Silicon-Diode detector (visible). The long- and short-wavelength

absorption edges are expected to occur at approximately 200 nm and 20 μm (Smakula, 1962; Touloukian and Dewitt, 1972), which are beyond the measurement range of this study. The measured properties agree with the expected behavior, which are indeed fairly uniform over the measured range and no absorption bands were detected. The properties are again not expected to vary significantly with temperature (Passerini, 2010), in particular because

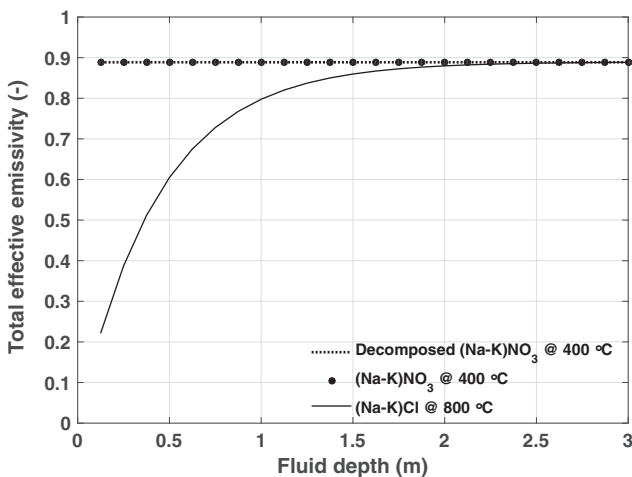


Fig. 9. Effective total emissivity of measured molten salt mixtures for different receiver fluid depths.

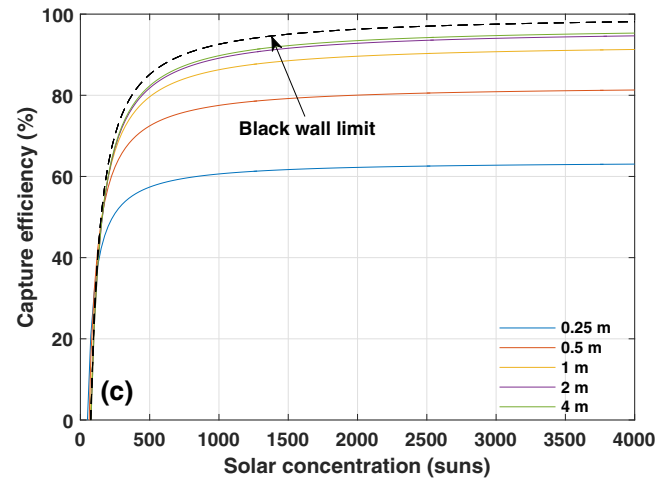
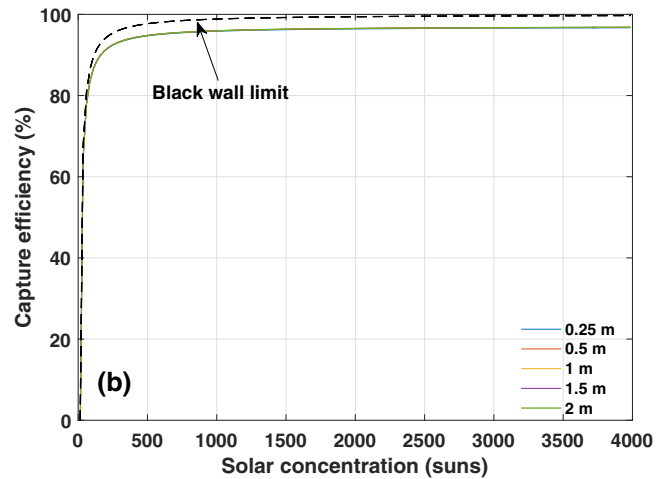
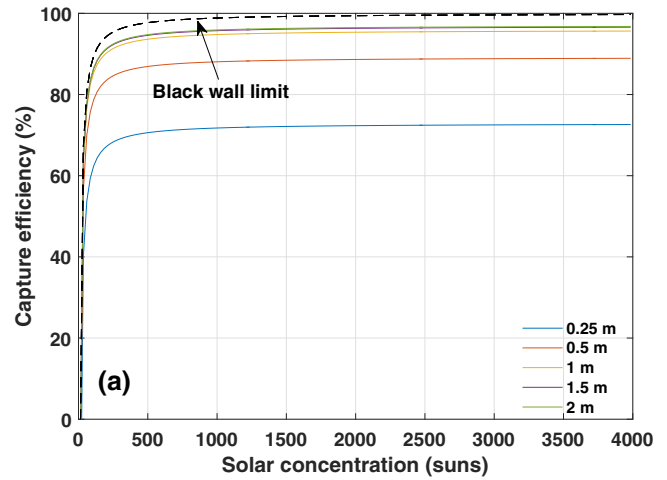


Fig. 10. Capture efficiency versus solar concentrations for fluid depths between 0.25 m and 2 m for binary nitrate (a), decomposed binary nitrate (b), and binary chloride (c).

the measured range is far away from the absorption edges where temperature dependence is most significant. Measurements were not possible beyond 2500 nm where the fluid is too transparent to be detected by the mid-infrared detector and linear extrapolation was applied for the analysis. The solar-weighted and re-emission-weighted absorption coefficients were determined to be $\kappa_{MS} = 2.5 \text{ m}^{-1}$ and $\kappa_{ME} = 0.7 \text{ m}^{-1}$, respectively. For the 1 m deep receiver example, the corresponding optical thicknesses are $\tau_{MS} = 5.0 \sim 1$ and $\tau_{ME} = 2.3 \sim 1$, indicating the absorbed solar irradiance is volumetrically distributed and the fluid behaves as a participating media in the re-emission spectrum at 800 °C (see Table 1).

The measured properties of all three liquids are summarized in Fig. 7 along with the normalized solar intensity spectrum and blackbody intensity spectra at 400 °C and 800 °C which highlight the behavior of each fluid in the relevant spectral ranges for solar receiver systems.

5. Discussion

5.1. Volumetric absorption

The volumetric absorption is visually and intuitively understood by the solar irradiance distribution at multiple depths in the candidate salts as illustrated in Fig. 8 for depths between 0 m and 2 m. The Figures show the absorption distribution for the initial irradiance penetration inside the fluid without reflection

contributions. The binary nitrate has well distributed absorption reaching >95% at 1 m. The binary chloride mixture also displays well distributed absorption, with 83% absorbed over a 0.5 m-depth and >95% at 2 m. Finally, the decomposed binary nitrate has very poor volumetric absorption performance and behaves as a surface absorber, with >95% absorbed within only 0.25 m. Since the spectral irradiance is effectively zero at all depths, its graphical representation was therefore omitted here. It is clear from these results that thermal decomposition will have significant consequences on the overall performance of the salts. The effects of thermal decomposition are therefore an important consideration in solar receiver design and lifetime analysis.

5.2. Effective emissivity

The total effective emissivity versus depth is presented in Fig. 9 for all three candidate salts. The total effective emissivity of both the unaffected and decomposed binary nitrates rapidly approaches an asymptotic value close to 0.9, with $\epsilon > 0.89$ for layers thicker than 2 cm. These results are readily predicted from the re-emission weighted optical thicknesses $\tau_{ME} \gg 1$ (see Table 1) indicating the fluids are optically thick in the re-emission region.

The total effective emissivity of the binary chloride for the range of fluid depths explored is much lower and requires over 1 m of fluid to reach values greater than 0.8. The results are fortuitous as they allow to offset the elevated emission losses associated with higher operating temperatures. Note that for the special case

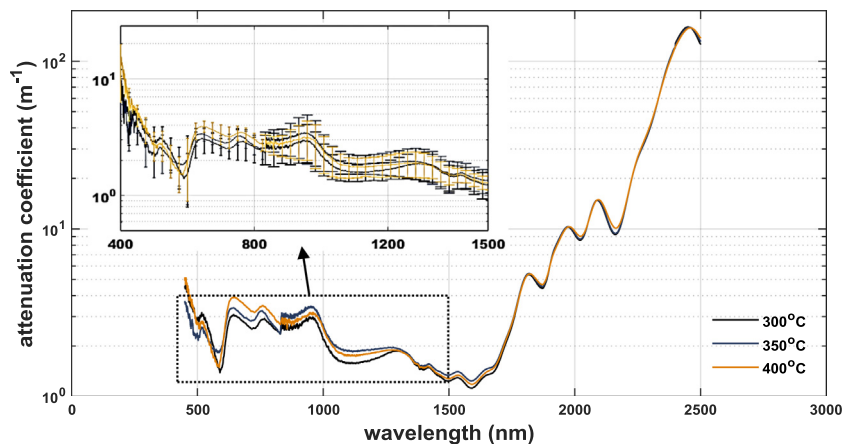


Fig. A.1. Absorption coefficient of 40 wt.% KNO_3 :60 wt.% NaNO_3 binary nitrate molten salt (SQM) at 300 °C, 350 °C, and 400 °C.

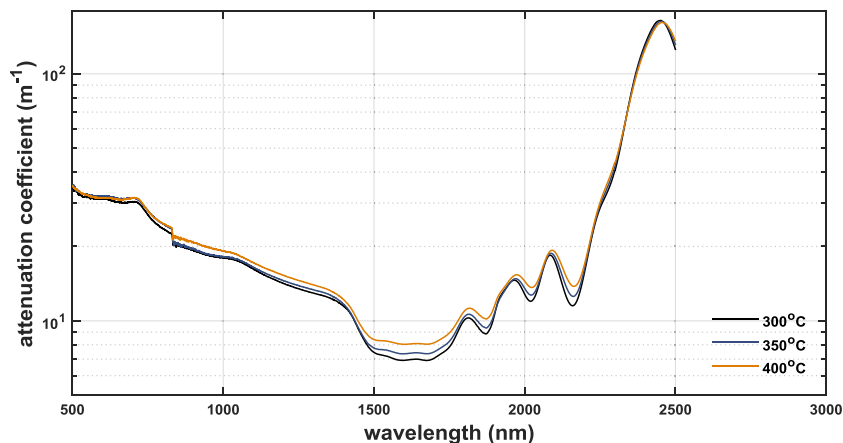


Fig. A.2. Absorption coefficient of decomposed 40 wt.% KNO_3 :60 wt.% NaNO_3 binary nitrate molten salt (SQM) at 300 °C, 350 °C, and 400 °C.

where the bottom boundary in Fig. 2 is a perfect absorber/emitter such that $\varepsilon_{j,bottom} = 1$, the total effective emissivity approaches approximately 0.9 for all fluids and fluid thicknesses for an isothermal layer.

5.3. Capture efficiency

The capture efficiencies, as defined in Section 2.4. (Eq. (10)), are presented in Fig. 10 for the candidate salt mixtures. The dashed line in each figure represents the maximum achievable capture efficiency in the case where the bottom boundary is “black” over the entire spectrum. This limit is independent of fluid thickness. Efficiencies are presented versus solar concentrations, with each curve representing a different total receiver fluid depth. Capture efficiency is independent of the fluid layer thickness for the decomposed binary nitrate due to the dominating surface absorption and blackbody radiator behaviors. High capture efficiencies >90% are therefore achieved at relatively low solar concentrations. The binary nitrate requires larger fluid thicknesses to achieve high efficiency due to the more gradual volumetric absorption. When the fluid is contained in a vessel with highly absorbing walls, capture efficiencies should approximately match those for the decomposed mixture.

The binary chloride operates at much higher temperatures and the lower total effective emissivity is not enough to offset the associated large radiative losses for low solar concentrations. For a 1 m layer of fluid, a solar concentration of 73 suns is required to “break even” (absorption = losses), 514-sun concentration yields an 80% capture efficiency, and 2250-suns achieves 90%. Similar to the nitrate salt, the performance of the chloride would improve with “black” containment vessel walls.

6. Conclusions

A method for measuring the absorption coefficient of nearly transparent, high temperature, non-scattering fluids was developed and tested. Comparisons to known absorption characteristics of some liquids were verified and the method was then used for characterizing molten salts. The properties of nitrate and chloride based salt mixtures were measured and the effects of thermal decomposition were investigated. A complete characterization of the thermal radiation performance in the solar and the re-emission spectra was presented and the behavior of the salts were discussed. The characterization can readily be used as a design tool for large-scale open receivers. The performance analysis demonstrates that a 1 m-deep volumetrically absorbing solar receiver with reflective containment walls and uniform temperature requires approximately 200 suns and 160 suns solar concentration to reach 90% capture efficiency for undecomposed and decomposed binary nitrate, respectively, and 2250 suns for binary chloride salts. Thermal decomposition was shown to have significant consequences on the performance of a binary nitrate mixture by reducing the depth of fluid required to absorb >95% of solar energy from approximately 1.0 m to 0.25 m, and effectively transforming the salt into an opaque surface absorber. Future work should focus on expanding the optical properties database of high temperature fluids to better identify optimal heat transfer fluid candidates.

Acknowledgements

This work was supported by the Cooperative Agreement between the Masdar Institute of Science and Technology (Masdar Institute), Abu Dhabi, UAE and the Massachusetts Institute of Technology (MIT), Cambridge, MA, USA – Reference 02/MI/MIT/C P/11/07633/GEN/G/00.

Appendix A. Effect of temperature on optical properties

The absorption coefficient versus wavelength for the SQM binary nitrate salt and the decomposed binary nitrate at 300 °C, 350 °C, and 400 °C are given in Figs. A.1 and A.2, respectively. Although it appears there could be a dependence on temperature for wavelengths less than 1500 nm, error bars overlap significantly and there is no clear trend.

Appendix B. Uncertainty analysis

$$\beta = \frac{-1}{\Delta x_{ji}} \ln \left(\frac{I_j}{I_i} \right) = \frac{-1}{\Delta x_{ji}} [\ln(I_j) - \ln(I_i)] \quad (\text{B.1})$$

$$\delta\beta = \sqrt{\left(\frac{\partial\beta}{\partial(\Delta x_{ji})} \delta(\Delta x_{ji}) \right)^2 + \left(\frac{\partial\beta}{\partial I_j} \delta I_j \right)^2 + \left(\frac{\partial\beta}{\partial I_i} \delta I_i \right)^2} \quad (\text{B.2})$$

$$\frac{\partial\beta}{\partial I_j} = \frac{-1}{I_j \Delta x_{ji}} \quad (\text{B.3})$$

$$\frac{\partial\beta}{\partial I_i} = \frac{1}{I_i \Delta x_{ji}} \quad (\text{B.4})$$

$$\frac{\partial\beta}{\partial(\Delta x_{ji})} = \frac{1}{(\Delta x_{ji})^2} \ln \left(\frac{I_j}{I_i} \right) \quad (\text{B.5})$$

$$\delta\beta = \sqrt{\left(\frac{1}{(\Delta x_{ji})^2} \ln \left(\frac{I_j}{I_i} \right) \delta(\Delta x_{ji}) \right)^2 + \left(\frac{-1}{I_j \Delta x_{ji}} \delta I_j \right)^2 + \left(\frac{1}{I_i \Delta x_{ji}} \delta I_i \right)^2} \quad (\text{B.6})$$

$$\delta I_j = \delta I_i = 0.1\% \quad (\text{B.7})$$

$$\delta(\Delta x_{ji}) = 0.5 \text{ mm} \quad (\text{B.8})$$

$$\delta\beta \cong \sqrt{\left(\frac{\delta(\Delta x_{ji})}{(\Delta x_{ji})^2} \ln \left(\frac{I_j}{I_i} \right) \right)^2} = \frac{\delta(\Delta x_{ji})}{\Delta x_{ji}} \beta \quad (\text{B.9})$$

Uncertainty dominated by the path length measurement uncertainty. The maximum uncertainty calculated from the experimental data, given that the smallest path length $\Delta x_{ji} = 10$ mm, is therefore

$$\frac{\delta\beta}{\beta} = \frac{\delta(\Delta x_{ji})}{\Delta x_{ji}} \leq 5\% \quad (\text{B.10})$$

Note that although intensity measurements were taken at 5 mm increments, the minimum path length difference was taken such that

$$\Delta x_{ji} = \Delta x_j - \Delta x_i = 10 \text{ mm}, 15 \text{ mm}, 20 \text{ mm}, \dots \quad (\text{B.11})$$

Appendix C. Reflectance calculation

The normal reflectance R_{norm} is given as

$$R_{norm} = \frac{1}{2} \left[\left(\frac{n_1 \cos \theta_2 - n_2 \cos \theta_1}{n_1 \cos \theta_2 + n_2 \cos \theta_1} \right)^2 + \left(\frac{n_1 \cos \theta_1 - n_2 \cos \theta_2}{n_1 \cos \theta_1 + n_2 \cos \theta_2} \right)^2 \right] \\ = \left(\frac{n-1}{n+1} \right)^2 \quad (\text{C.1})$$

where n_1 and n_2 are the refractive indices in the liquid and air, respectively. Taking $\theta_1 = \theta_2 \approx 0$, and letting $n_1 = n$ and $n_2 = 1$, yields

$$R_{norm} = \left(\frac{n-1}{n+1}\right)^2 \quad (C.2)$$

The diffuse, hemispherical reflectance R_{diff} is given as

$$R_{diff} = 1 - \frac{1}{2}(\epsilon_{\parallel} + \epsilon_{\perp}) \quad (C.3)$$

$$\epsilon_{\parallel} = \frac{8}{n^2 + k^2} \left(1 - \frac{n}{n^2 + k^2} \ln[(n+1)^2 + k^2] + \frac{(n^2 - k^2)}{k(n^2 + k^2)} \tan^{-1} \frac{k}{n+1} \right) \quad (C.4)$$

$$\epsilon_{\perp} = 8n \left(1 - n \ln \frac{(n+1)^2 + k^2}{n^2 + k^2} + \frac{(n^2 - k^2)}{k} \tan^{-1} \frac{k}{n(n+1) + k^2} \right) \quad (C.5)$$

where k is the absorptive index in the complex index of refraction, with $n \gg k$ in semi-transparent liquids. Taking the limit as $k \rightarrow 0$, we obtain after applying L'Hôpital's rule and some math,

$$\lim_{k \rightarrow 0} \epsilon_{\parallel} = \frac{8}{n} \left(1 - \frac{2}{n} \ln(n+1) + \frac{1}{n+1} \right) \quad (C.6)$$

$$\lim_{k \rightarrow 0} \epsilon_{\perp} = 8n \left(1 - 2n \ln \frac{n+1}{n} + \frac{n}{n+1} \right) \quad (C.7)$$

and

$$\lim_{k \rightarrow 0} R_{diff} = 1 - \frac{4}{n} \left(1 - \frac{2}{n} \ln(n+1) + \frac{1}{n+1} \right) - 4n \left(1 - 2n \ln \frac{n+1}{n} + \frac{n}{n+1} \right) \quad (C.8)$$

References

- Alqaydi, M.S., Delclos, T., Almheiri, S., McKrell, T., Calvet, N., 2016. Effect of sand and moisture on molten salt properties for open direct absorption solar receiver/storage system. In: AIP Conference Proceedings. <http://dx.doi.org/10.1063/1.4949100>.
- ASTM Standard G173-03, 2003. Standard tables for reference solar spectral irradiances: direct normal and hemispherical on 37° tilted surface.
- Bloom, H., Rhodes, D.C., 1956. Molten salt mixtures. Part 2. The refractive index of molten nitrate mixtures and their molar refractivities. *J. Phys. Chem.* 60, 791–793. <http://dx.doi.org/10.1021/j150540a022>.
- Drotning, W.D., 1978. Optical properties of solar-absorbing oxide particles suspended in a molten salt heat transfer fluid. *Sol. Energy* 20, 313–319. [http://dx.doi.org/10.1016/0038-092X\(78\)90123-8](http://dx.doi.org/10.1016/0038-092X(78)90123-8).
- Gil, A., Codd, D.S., Zhou, L., Trumper, D., Calvet, N., Slocum, A.H., 2016. Concentrated solar power on demand demonstration: construction and operation of a 25 kW prototype. *AIP Conf. Proc.* 1734. <http://dx.doi.org/10.1063/1.4949115>.
- Howell, J.R., Menguc, M.P., Siegel, R., 2010. *Thermal Radiation Heat Transfer*. CRC Press.
- Hutchings, D.C., Sheik-Bahae, M., Hagan, D.J., Van Stryland, E.W., 1992. Kramers-Kronig relations in nonlinear optics. *Opt. Quant. Electron.* 24, 1–30. <http://dx.doi.org/10.1007/BF01234275>.
- Janz, G.J., 1967. *Molten Salts Handbook*. Academic Press, New York.
- Jindal, H., Harrington, G., 1967. Refractometry in fused alkali nitrates and thiocyanates. *J. Phys. Chem.* 71 (6), 1688–1694.
- Khullar, V., Tyagi, H., Hordy, N., Otanicar, T.P., Hewakuruppu, Y., Modi, P., Taylor, R. A., 2014. Harvesting solar thermal energy through nanofluid-based volumetric absorption systems. *Int. J. Heat Mass Transf.* 77, 377–384. <http://dx.doi.org/10.1016/j.ijheatmasstransfer.2014.05.023>.
- Kramers, H.A., 1927. La diffusion de la lumiere par les atomes. *Atti Congr. Int. Fis. Como* 2, 545.
- Kronig, R., 1926. On the theory of dispersion of X-rays. *J. Opt. Soc. Am.* 12, 547–557.
- Lenert, A., Wang, E.N., 2012. Optimization of nanofluid volumetric receivers for solar thermal energy conversion. *Sol. Energy* 86, 253–265. <http://dx.doi.org/10.1016/j.solener.2011.09.029>.
- Lorentz, H.A., 1935. The radiation of light. In: *Collected Papers*. Springer, pp. 17–27.
- Makino, T., Maeda, T., Edamura, M., Yasuo, T., Yoshida, A., 1991. Thermal radiation properties of molten salts (properties of alkali metal chlorides and conductive-radiative transfer in the salts). *Heat Transf. Jpn. Res.* 20, 711–721.
- Modest, M.F., 2013. *Radiative Heat Transfer*. Academic Press, Oxford.
- Myers, P.D., Yogi Goswami, D., Stefanakos, E., 2015. Molten salt spectroscopy for quantification of radiative absorption in novel metal chloride-enhanced thermal storage media. *J. Sol. Energy Eng.* 137, 41002. <http://dx.doi.org/10.1115/1.4029934>.
- Ni, G., Li, G., Boriskina, S.V., Li, H., Yang, W., Zhang, T., Chen, G., 2016. Steam generation under one sun enabled by a floating structure with thermal concentration. *Nat. Energy* 1, 16126. <http://dx.doi.org/10.1038/nenergy.2016.126>.
- Otanicar, T.P., Phelan, P.E., Golden, J.S., 2009. Optical properties of liquids for direct absorption solar thermal energy systems. *Sol. Energy* 83, 969–977. <http://dx.doi.org/10.1016/j.solener.2008.12.009>.
- Passerini, S., 2010. *Optical and Chemical Properties of Molten Salt Mixtures for Use in High Temperature Power Systems*. Massachusetts Institute of Technology.
- Passerini, S., McKrell, T., 2012. A facile apparatus for the high temperature measurement of light attenuation in nearly transparent liquids/molten salts. *J. Nanofluids* 1, 78–84. <http://dx.doi.org/10.1166/jon.2012.1010>.
- Slocum, A.H., Codd, D.S., Buongiorno, J., Forsberg, C., McKrell, T., Nave, J., Papanicolas, C.N., Ghobeity, A., Noone, C.J., Passerini, S., Rojas, F., Mitsos, A., 2011. Concentrated solar power on demand. *Sol. Energy* 85, 1519–1529. <http://dx.doi.org/10.1016/j.solener.2011.04.010>.
- Smakula, A., 1962. Synthetic crystals and polarizing materials. *Opt. Acta* 9, 205–222. <http://dx.doi.org/10.1080/713826427>.
- Touloukian, Y.S., Dewitt, D.P., 1972. Thermal radiative properties, nonmetallic solids, thermophysical properties of matter 8, IFL.
- Viskanta, R., Anderson, E.E., 1975. Heat transfer in semitransparent solids. *Adv. Heat Transf.* 11, 317–441.
- Webb, B.W., Viskanta, R., 1985. Analysis of heat transfer and solar radiation absorption in an irradiated thin, falling molten salt film. *J. Sol. Energy Eng.* 107, 113. <http://dx.doi.org/10.1115/1.3267663>.